Compensation of heat deformations by adaptive optics for the ALS upgrade

Manuel Sanchez del Rio,[a] Antoine Wojdyla,[a]* Kenneth A. Goldberg,[a] Grant D. Cutler,[a] Daniele Cocco[a] and Howard A. Padmore[a]

[a]LBNL, 1 Cyclotron Road, Berkeley CA, USA. Correspondence e-mail: awojdyla@lbl.gov

We develop a realistic wave optics simulation method to study how wavefront distortions originated by heat load deformations can be corrected using adaptive X-ray optics. Several planned soft X-ray and tender X-ray insertion-device beamlines in the Advanced Light Source upgrade rely on a common design principle. A flat, first mirror intercepts the white beam; vertical focusing is provided by a variable-line-space monochromator; and horizontal focusing comes from a single, pre-figured, adaptive mirror. A variety of scenarios to cope with thermal distortion in the first mirror are studied by finite-element analysis. We analyze the degradation of the intensity distribution at the focal plane and model the adaptive optics that correct it. We report the range of correctable wavefront errors across the operating range of the beamlines in terms of mirror curvature and spatial frequencies. The software developed is a one-dimensional wavefront propagation package made available in the OASYS suite, which is an adaptable, customizable and efficient beamline modeling platform.

1. Introduction

Quantitative calculation and evaluation of the parameters related to X-ray optics are of great importance for designing, building and exploiting new beamlines. These calculations allow testing of the design parameters in a virtual computer environment where advantages and limitations can be simulated accurately. The optics imperfections play a fundamental role in the simulations and often constitute the limiting factor of the beamline performances. Deformations of the optical elements due to heat load need to be always controlled and in some cases corrected, therefore optics simulations and engineering modeling of the thermal deformations by finite element analysis (FEA) have to be developed in parallel.

Simulations of the beamline optics can be done in different degrees of approximation and effort, starting using analytical formulas, performing ray tracing and also wavefront propagation (Sanchez del Rio *et al.*, 2019). Different packages for such simulations are available in the OASYS suite (Rebuffi & Sanchez del Rio, 2017*b*). For incoherent photon beams, the ray tracing technique is enough for most purposes. If the X-ray beam is highly coherent, like in soft X-ray beamlines of the upgraded ALS facility discussed in this paper, a pure wave optics simulation is sufficient. For hard X-rays, where the coherent fraction for upgraded facilities is usually a few percent, simulations require using hybrid methods (Shi *et al.*, 2014) or more sophisticated partial coherence algorithms such as Monte Carlo sampling (Chubar *et al.*, 2011) and Coherent Mode Decomposition (Glass, 2017).

A common setup to be implemented in several beamlines at the Upgraded Advanced Light Source (ALS-U) consists in a horizontal deflecting cooled plane mirror M1 to absorb a large part of the white beam power, followed by a horizontally focusing adaptive mirror M3, which focus and corrects wavefront errors. A variable-line-space (VLS) grating monochromator is placed in between to disperse and focus the beam in the vertical plane (Reininger & de Castro, 2005), which is decoupled from the M1-M3 system. In this paper we study the ability of the adaptive mirror M3 to compensate for wavefront distortions caused by power load in M1. The white beam impinges on M1 after beam shaped by the high power slits, but the power released in the mirror system may produce significant deformation of the mirror surface that degrades the beam quality. A variety of thermal distortion scenarios were implemented from finite-element analysis (FEA) models using realistic undulator power spectra and cooling strategies under consideration by the project. In the case of interest of ALS-U, the coherent fraction is high enough to justify a full coherent optics calculation (about 0.8 for the case under study, a 4 m undulator at 250 eV). Moreover, in this case, as most times in synchrotron beamlines, the optics in the horizontal and vertical planes are decoupled thus a separated modeling of the horizontal and vertical planes is justified. The 1D modeling is orders of magnitude less demanding in computational resources than the 2D calculations, therefore it is always recommended to start a wave optics simulation in its simpler 1D form. We present here the fundamentals of a 1D wave propagation model implemented in the WOFRY (Rebuffi & Sanchez del Rio, 2017*a*) tool in OASYS.

The 1D waveoptics propagation model is also well adapted to study optimization problems, because a parametric study (scan of a single variable) or multiple optimization require running many single simulations. In our case, the M3 correction profile is optimized and expressed as a function of the input signal

required by the actuators that shape the optics. Using data from a 20-channel adaptive X-ray mirror prototype we implemented mirror shape-control algorithms designed to restore and optimize the focused beam intensity (i.e., Strehl ratio).

The paper is organised as follows: we first describe the methods and algorithms implemented in the WOFRY 1D simulations concerning the sources, wave propagators for free space, and optical elements and (section 2). In section 3 we describe the system under study, that corresponds to the parameters of the FLEXON beamline at ALS-U. The FEA results for M1 in terms of surface deformation originated by absorbed power are discussed. We show (section 3.4) how the adaptive X-ray optics (AXO) can compensate the errors using an ad-hoc computed mirror profile compatible with the AXO control system. In section 4 the complete beamline is simulated using a 1D wavefront propagation model by combining the results of the horizontal and vertical planes. A final summary is in section 5.

2. Simplified 1D wavefront modeling for a synchrotron beamline

A wavefront simulation consists in the creation of a wavefront with some characteristics (geometry, wavelength), its propagation in free space and its modification by the optical elements (slits, mirrors, etc). We restrict here to a 1D model in the (x, y) plane, being y the propagation direction (optical axis) and x the direction transverse to the beam propagation to analyze (usually the of horizontal or vertical plane). The wavefront is represented by the electric field of a monochromatic component (angular frequency ω, wavelength λ, wavenumber $k = 2\pi/\lambda$ or photon energy W) at a position $y=0$ along the propagation direction. This electric field or electric disturbance is a complex scalar $E(x; y = 0, \omega)$ or, in case of polarized beams two complex scalars, one for σ and the other for π polarization. The wavefront intensity is the square of the modulus of the amplitude: $I = |A \exp(i\phi)|^2 = A^2$.

2.1. Modeling sources

2.1.1. Simple waves: plane, spherical and Gaussian The simplest wavefront corresponds to a plane wave, that has constant complex amplitude for any x coordinate:

$$E(x; y = 0, \omega) = E_0 = A_0 e^{i\phi_0}, \tag{1}$$

where E_0 is a complex value that can be expressed in its constant real amplitude A_0 and a constant phase ϕ_0. A plane wave is infinite along the x direction. However, when implementing a wavefront in a computer the electric field has to be sampled over an array of discrete values of complex amplitude, and they are necessarily defined over a finite x interval.

A spherical wave (strictly speaking a circular wave in 1D, but we keep the terminology used in 2D) has a constant complex amplitude over a sphere of a given radius R. Obviously it cannot be represented at the source point ($y = 0$, center of the sphere) and our wavefront must be sampled at a given distance $y = R$ and over a line perpendicular to the radius and tangent to the sphere. At $x = 0$ (a point in the sphere) the field has a constant value equal to the value at the surface. But at a $x \neq 0$,

over a range of x-values $x << R$ (small numerical apertures) the distance from x to the sphere parallel to the y direction gives an optical path that modifies the phase by $k \Delta x$. It is easy to deduce that the wavefront in the line tangent to the sphere has the expression

$$E(x; y = R, \omega) = E_0 e^{ikx^2/(2R)}. \tag{2}$$

A Gaussian beam has intensity following a Gaussian distribution with standard deviation σ_I, thus the electric disturbance is:

$$E(x; y = 0, \omega) = E_0 e^{-x^2/(4\sigma_I^2)} \tag{3}$$

2.1.2. A simplified model for the Undulator source A single electron (or filament beam) traveling in an undulator with pure sinusoidal magnetic field in one direction will produce a complicated wavefront with geometry that varies as a function of the photon frequency (see, e.g., Ref. (Onuki & Elleaume, 2003)). At the resonance energy the angular emission in the far field can be approximated by a Gaussian of width (Onuki & Elleaume, 2003)

$$\sigma_u' \approx \sqrt{\frac{\lambda}{2L}}, \tag{4}$$

with λ the wavelength of the photons at the undulator resonance and L the undulator length. At the source point, the size of the source can also be approximated by a Gaussian of

$$\sigma_u \approx \sqrt{\frac{\lambda L}{2\pi^2}} = \frac{\lambda}{2\pi}\frac{1}{\sigma'}. \tag{5}$$

A simplification of the undulator radiation in the far field consists in a spherical wave (Eq.2) with origin in the undulator center modulated with an amplitude that follows the Gaussian in Eq. 4, therefore

$$E(x; y = y_0, \lambda) = E_0 e^{ikx^2/(2y_0)} e^{-x^2/(4\sigma_u'^2 y_0^2)}. \tag{6}$$

A second way to simulate the undulator is considering a Gaussian source as defined in Eq. 3 with $\sigma_I = \sigma_u$. Note that propagating this approximation of the undulator as a Gaussian source to a screen at $y = y_0$ does not reproduce the result in Eq. 6 because Gaussian propagation implies a product of sigmas (emittance) of $\lambda/(4\pi)$ whereas for undulator radiation the emittance is approximately $\lambda/(2\pi)$ (Eq. 5). For practical purposes, the Gaussian source approximation can be used for optical systems accepting a high numerical aperture (NA) whereas for systems of small NA the spherical way approximations may be preferred.

2.2. Modeling propagation in free space

For simulating the beamline, the wavefront at the source has to be created using the methods in Section 2.1, and the iterative effect of the optical elements has to be simulated using the results in the next section 2.3. But the wavefront changes when transported in free space from element to element. We use here two propagators.

2.2.1. Direct implementation of integral Rayleigh-Sommerfeld propagator

The Rayleigh-Sommerfeld propagator for small-angle approximation expresses the electric field at a spatial point $\vec{r}'$ as an integral of the electric field at a spatial point $\vec{r}$ (Goodman, 2017)

$$E(\vec{r}') = \frac{k}{2\pi i} \int \frac{E(\vec{r})}{|\vec{r}' - \vec{r}|} e^{ik|\vec{r}' - \vec{r}|} d\Sigma, \qquad (7)$$

where the integral is made over the domain of the source (the surface Σ). This propagator can be applied to numerical discrete 1D wavefronts, and the integral reduces to a sum

$$E(x_1, y_1) \approx \frac{k}{2\pi i \Delta y} \sum_{i=0}^{N-1} E(x_{0,i}, y_{0,i}) e^{ik\sqrt{(x_1 - x_{0,i})^2 + (y_1 - y_{0,i})^2}} \Delta x_0, \qquad (8)$$

where Δy is the mean value of the denominator in the integral in Eq. 7. Note that one sum over the N points of the sampled incident wavefront has to be done for each coordinate at the transported wavefront, thus the number of operations is of the order N^2. This simple propagator gives flexibility to define different gridding and limits and even non parallel planes for the incident and transported wavefronts, permitting to adjust the window and resolution when working with converging or divergent wavefronts.

2.2.2. Fresnel propagator using FFT: The zoom propagator

By making a Taylor expansion of the quadratic phase in Eq. 7 the Fresnel propagator is obtained:

$$E(x; y_1) = \frac{e^{ik(y_1 - y_0)}}{\sqrt{i\lambda(y_1 - y_0)}} \int E(x'; y_0) e^{\frac{ik}{2(y_1 - y_0)}(x - x')^2} dx'. \qquad (9)$$

The Fresnel integral propagator can be seen as convolution of the wavefield with a Gaussian kernel. One can write Equation 9 in convolution form, involving two-Fourier transforms:

$$E(x; y_1) = \mathcal{F}^{-1}\left\{\mathcal{F}\{E(x; y_0)\} \times e^{-i\pi\lambda(y_1 - y_0)u^2}\right\}, \qquad (10)$$

where the exponential function comes from the back-Fourier of the exponential inside the integral in Eq. 9, being u the conjugated variable of x. The real benefit of using this scheme comes from the use of Fast Fourier Transforms, that reduce the number of operations from N^2 to $N\log_2 N$. Its use is essential when doing simulations in 2D, because the direct calculation of the integral lead to N^4 operations at the limit of calculation power of usual laptop computers. However, the FFT implementation requires that the gridding and window of the incident and transported wavefronts must be equal. This is a problem when a wavefront is propagated to a focal point: the gridding of the incident wavefront used at the image provides a poor resolution because most of the intensity is concentrated in a very few pixels. A clever solution to this problem is presented by J.D. Schmidt (Schmidt, 2010) that makes possible to calculate the propagated field in a "zoomed" window, thus permitting optimizing the wavefront sampling in cases for propagating highly convergent or divergent wavefronts. The problem reduces to a convolution problem of the unpropagated field field $E(x; y_0)$ affected by a phase P with a kernel K, and the result affected by a global phase P^G:

$$E(x; y_1) = P^G \mathcal{F}^{-1}\left\{\mathcal{F}\{E \ P\}K\right\}, \qquad (11)$$

where

$$P^G = \frac{e^{ik(y_1 - y_0)}}{\sqrt{m_x}} e^{i\frac{k}{2(y_1 - y_0)} \frac{m_x - 1}{m_x} x_2^2}, \qquad (12)$$

$$P = e^{i\frac{k}{2(y_1 - y_0)}(1 - m_x)x_1^2}, \qquad (13)$$

$$K = e^{-i\pi\lambda(y_1 - y_0)\frac{u^2}{m_x}}. \qquad (14)$$

The term m_x is the magnification (zoom) factor. Note that setting one magnification $m_x = 1$ one obtains the standard Fresnel propagator (Eq. 10).

2.3. Modeling optical elements

In some cases, the optical elements can be considered in a good approximation as thin elements (zero thickness along the y axis), therefore their effect can be encapsulated in a complex transmission amplitude

$$R(x; \omega) = r(x; \omega)e^{i\rho(x,\omega)}. \qquad (15)$$

Therefore, the wavefield after an optical element placed at position $y = y_0$ will be the wavefield at y_0 just before the interaction multiplied by the complex transmission:

$$E'(x; y = y_0, \omega) = E(x; y = y_0, \omega)R(x; \omega) \qquad (16)$$

2.3.1. Apertures (slits, beamstops and element dimension)

A generic aperture is a mask that transmits a part of the wavefront in a range $[x_{min}, x_{max}]$ and absorbs the rest. It can be

$$R(x; \omega) = \begin{cases} A & \text{if } x_{min} \leq x \leq x_{max} \\ 1 - A & \text{elsewhere} \end{cases} \qquad (17)$$

When the element is a slit, then $A = 1$. If it is a beamstop, then $A = 0$. If we deal with an optical element of finite length L placed at a grazing incidence angle θ, it acts as a slit of aperture equal the projection of the length on the x axis: $A = 1$, $x_{min} = -(L/2)\sin\theta$ and $x_{max} = (L/2)\sin\theta$.

2.3.2. Ideal lens

We can define an ideal lens as a focusing device that converts a plane wave into a spherical wave collapsing to the focus at a distance f from the ideal lens position. Therefore

$$R(x; \omega) = e^{-ik \ x^2/(2f)} \qquad (18)$$

2.3.3. Ideal reflector

Let us consider a perfectly reflecting surface (no absorption) with a profile $h(w)$ with h the elevation (height) and w the linear coordinate in a reference frame attached to the reflector with origin in the reflector's center. A plane reflector has $h(w) = 0$ and, for example, a circular mirror of radius R has $h(w) = R - \sqrt{R^2 - w^2}$. The profile $h(w)$ can also match a deformation originated for instance by heat load or a mirror surface error (waviness).

If the reflector is set with an incident angle θ with the propagation axis y, the change of optical path is $\Delta y =$

$2h(x/\sin\theta)\sin\theta$ with a consequent phase shift $\Delta\Phi = -k\Delta y$, therefore for the ideal reflector

$$R(x;\omega) = e^{-2ikh(x/\sin\theta)\sin\theta}. \tag{19}$$

This model of ideal reflector as a thin object can be used for any reflecting shape (circular, ellipse) but the intrinsic aberrations are not correctly considered. For example. if we consider a circular mirror, then $h(w) \approx (1/2)(w/R)^2$ and when inserted in Eq. 19 it introduces a quadratic phase thus focusing perfectly a plane wave into a collapsing spherical wave. We know this is not true as there are aberration (spherical aberration, coma, etc.) that are ignored by this model. The main reason is the incidence angle θ, which is not constant along the mirror profile thus Eq. 19 is not exact. A model for a "grazing reflector" that solves this problem is presented in the next Section 2.3.4.

A reflector of a finite size can be decomposed in two elements, the ideal reflector described here followed (or preceded) by the aperture as described in 2.3.1.

2.3.4. Grazing reflector The method used for the *ideal reflector* does not account for mirror aberrations and also has problems with dealing with mirror errors. These effects are more important for elements in grazing incidence, where the *thin object* approximation is not valid. A solution for that consists in using the propagator in Sec. 2.2.1 to propagate the incident wavefront until the points in the mirror surface (w, h). Let be p the distance from the wavefront $E_0(x, ; y = 0, \omega)$ to the center of the mirror placed at a grazing incidence θ with the optical axis. In the mirror reference frame, the wavefront coordinates are $(w_s, h_s) = (-p\cos\theta, p\sin\theta) + (x\sin\theta, x\cos\theta,)$. It is straightforward to extend the integral propagator (Eq. 8) to calculate the propagated field at the surface points (w, h) by summing over all points of the input wavefront. Once known the electric perturbation at the mirror surface, another propagation is done using the same principle to the image plane placed at a distance q from the mirror center.

2.3.5. Gratings A grating produces a deflection of the incident beam that is dependent on its wavelength. It is expressed by the grating equation is

$$m\lambda g = \sin\alpha + \sin\beta, \tag{20}$$

with α is the incidence angle (measured with respect to the normal), β is the reflection angle, with opposite sign of α if it lies at the other side of the normal, m the diffraction order (positive for inside reflection, i.e., $\alpha \geq |\beta|$), λ is the photon wavelength, and g is the grating groove density, which is a function of w for VLS gratings: $g = g_0 + g_1 w + g_2 w^2 + ...$ with $g_0 = 1/d_0$ the lines per unit of length at the grating center (d_0 the distance between two grating lines).

The simulation of a grating using a thin object model (Eq. 19) is difficult because in addition to the geometric optical path it is necessary to account for the wavelength-dependent component. We use here an approach that is exact, except for accounting for grating efficiency, which consisting in sampling the grating as a numeric mesh and apply the "grazing reflector". It is important not to undersample the grating (e.g., include several points per period) and orientate the incident and image wavefronts with the correct angles α and β.

3. Simulation of ALS-U generic undulator beamline

Four new undulator beamlines are being designed for the ALS-U project. The different scientific cases imply particular selection of the insertion devices and beamline optics. However, most of the beamlines (or beamline branches) follow a similar scheme: 1) undulator source, 2) white beam flat mirror M1 deflecting horizontally, 2) plane mirror M2 vertically deflecting to work in tandem with the grating, 3) a VLS (varied line spacing) grating that disperses vertically the beam and focus it in the exit slit, and 4) an elliptical mirror M3 deflecting in the horizontal plane and focusing horizontally on the exit slit. The mirror M3 is equipped with a bimorph adaptive system that permits, in association with a wavefront sensor, to correct wave deformations introduced upstream of it.

The goal of this paper is to study whether this AXO permits to correct the distortions produced by the heating and deformation of M1.

The total power P emitted by an undulator is

$$P[W] = 72.5688(E_e[GeV])^2 I[A] N_u K^2 / \Lambda[mm], \tag{21}$$

where K is the undulator deflecting parameter, N_u the number of periods, Λ the undulator period, I is the storage ring current, and E_e is the storage ring energy. From this equation we can deduce that the maximum of power is obtained at maximum of K corresponding to the minimum of the energy for a given harmonic. We have selected the case of the FLEXON beamline because the insertion device delivers a high power and the beamline design follows the structure already described. Therefore, it constitutes the worst case that requires the most demanding actions to minimize the deformations (in M1) and correct the distortions (in M3). The FLEXON beamline will incorporate a Delta undulator (Temnykh *et al.*, 2011) with $\lambda = 28.8$ mm, $N_u = 137$ and $K_{max} = 3.07$, emitting a total power of $P = 6507$ W in ALS-U ring (2 GeV, 0.5 A).

3.1. Deformation of M1 due to heat load

The white beam mirror M1 is placed at a distance 13.73 m from the source, has a grazing angle of 1.25, and is gold coated. The distribution of the heat load on the mirror depends on undulator parameters (deflection parameter horizontal K_h, vertical K_v and phase Φ). Depending on the polarization wanted, these parameters take different values (horizontal linear polarization $K_h = 0$, vertical linear polarization $K_v = 0$, linear polarizartion at $45 K_h = K_v$, $\Phi = 0$, circular polarization $K_h = K_v$, $\Phi = 90$). In Fig. 1 the incident power density on the M1 mirror surface is plotted for $K = \sqrt{K_h^2 + K_v^2} = 3.07$ in various polarization states.
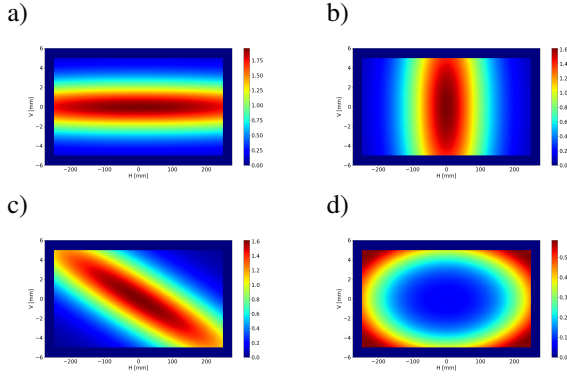
Figure 1
Power density (in W/mm^2) on mirror M1. a) $K_h = 3.07, K_v = 0$ (integrated power 3523 W), b) $K_h = 0, K_v = 3.07$ (integrated power 3776 W), c) $K_h = 2.171, K_v = 2.171, \Phi = 0$ (integrated power 3978 W), d) $K_h = 2.171, K_v = 2.171, \Phi = 90$ (integrated power 1353 W).

In order to calculate the absorbed power density at the mirror, it is necesary to apply the energy-dependent mirror reflectance on the power density for different energies. There are several codes that can be computed this, like SPECTRA (Tanaka & Kitamura, 2001), SRCALC-IDPOWER (Reininger, 2001) and XOPPY. The last two codes are available in the OASYS environment. Table 1 shows the results in terms of power absorbed and peak power density as calculated by these three codes.

Table 1
Absorbed power by the mirror M1 in different apertures as calculated by different codes. [TODO: "remove incomplete tables V and Circ"]

H polarization	SPECTRA	SRCALC	XOPPY
Power (W) in 500×10 mm^2	2070	2489	2347
Power (W) in 100×2.4 mm^2	239	306	245
Peak power density (W/mm^2)	1.01	1.26	1.18

V polarization	SPECTRA	SRCALC	XOPPY
Power (W) in 500×10 mm^2	Grant?	2319	-
Power (W) in 100×2.4 mm^2	Grant?	292	-
Peak power density (W/mm^2)	Grant?	1.24	-

Circ polarization	SPECTRA	SRCALC	XOPPY
Power (W) in 500×10 mm^2	-	535	-
Power (W) in 100×2.4 mm^2	-	3.14	-
Peak power density (W/mm^2)	-	0.42	-

The distortion of the mirror was calculated using the finite element method, as implemented in the ANSYS software. The result of the finite element calculation is a map of the surface deformation for a given heat load and mirror design. Fig. 2 shows the deformation maps (column 1) and the extracted profile (column 2). The maps were loaded in OASYS using a dedicated widget that also extracts the 1D profile and send it to the reflector.

We calculated distortions for two different cooling schemes: a water-side-cooled mirror and a liquid-nitrogen-cooled mirror [TODO: "ref paper on this, Cutler et. al."]. Both mirrors are made from single-crystal-silicon substrates. In the case of the

water-side-cooled mirror, we controlled distortion by a combination of mirror design parameters, specifically beam overfilling, a notched or smart-cut substrate, and tuned cooling length (Zhang *et al.*, 2013) [TODO: "Grant: do you agree with this ref?"]. Note that we did not optimize these parameters for to minimize height or slope error, but instead chose parameters for a range of heat loads, and to facilitate adaptive correction.

It is important to note that our water-cooled finite element model does not include a mounting or cooling system, and therefore the presented results should be seen as a 'best' or idealized case. In other words, the shape of an actual water-cooled mirror will be more difficult to correct than what the calculations in this model indicate. In contrast, our model of the liquid-nitrogen-cooled mirror does includes mounting and cooling system deformation, and therefore is a more realistic model than what is presented for the water-side-cooled case.
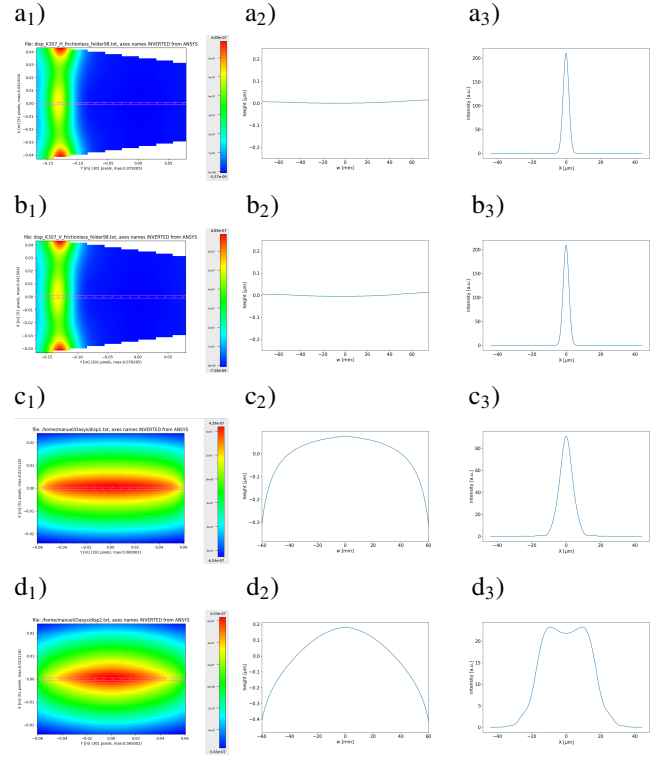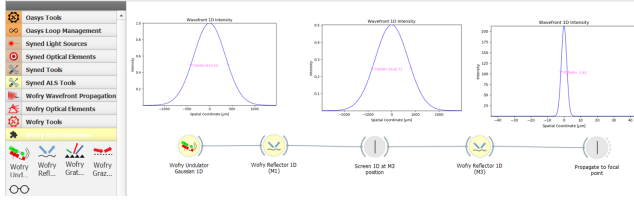

Figure 2
Left column: 2D map of the surface deformation: a$_1$) cryogenic mirror for $K_h = 3.07$, $K_v = 0$; b$_1$) cryogenic mirror for $K_h = 0$, $K_v = 3.07$; c$_1$) water-cooled mirror $K_h = 3.07$, $K_v = 0$; d$_1$) water-cooled mirror $K_h = 0$, $K_v = 3.07$. Central column: the extracted 1D profiles a$_2$,b$_2$,c$_2$, and d$_2$ respectively. Right column: The focused image with these profiles are in Figs. a$_3$, b$_3$, c$_3$ and d$_3$, respectively. The FWHM values are: 3.85, 3.91, 8.53 and 36.34μm, respectively (3.68 μm for the undeformed one) and the Strehl ratios: 0.99, 0.98, 0.43 and 0.11, respectively (one for the undeformed mirror).

3.2. Beamline simulation and effect of M1 deformation

The beamline simulation has been performed using WOFRY. The undulator field is calculated at a position just before M1 (y=13.73 m) using the model described in Section 2.1.2. M1 is a plane reflector that accepts a deformation profile. We first

studied the case of no deformation. The wavefront is propagated from M1 to a distance 13.599 m in free space until M3 position using the zoom propagator (Section 2.2.2). Then M3 implements a reflector with a radius $R = 220.72$ m obtained from the lens equation $1/p + 1/q = 1/f = 2/(R \sin(\theta))$ with $p = 13.73 + 13.599$, $q = 2.64$, $\theta = 1.25$. With no deformation in M1 the image has a full-width at half maximum of 3.84 μm (Fig. 3 and an intensity of 213 in arbitrary units, which will be then used to normalize intensities with the non-deformed case and calculate the Strehl ratio

Figure 3
OASYS workspace showing the simulation for the beamline with no deformation in M1. The intensity profile of the beam are superposed at different positions, with FWHM of 819μm at M1, 1631μm at M3 and 3.82μm at the focal position.

The results for the different mirror deformations in M1 are: for the cryogenically cooled mirror there is no significant degradation of intensity distribution of the image, increasing slightly the width (3.85μm and 3.91μm for the beam horizontally (H) and vertically (V) polarized, respectively) when compared with the undeformed calculation (3.82μm). There is a small degradation in the Strehl ratio (0.99 for H polarization and 0.98 for V) (column 3 in Fig. 2). For the case of water cooled mirror the situation changes: The focal spot degraded to a FWHM=8.53 μm for H polarization and 36.34μm for V polarization, with a consequent Strehl ratio of 0.43 (H) and 0.11 (V), values that are unacceptable for most applications.

We can conclude that the cryogenic cooling is almost perfect in the sense that it does not alter the intensity distribution with optimum Strehl ratios. The deformation in the water cooled mirrors produces a large deterioration of the intensity profile for both cases of polarization. The associated Strehl ratio are far away from what is usually accepted (larger than 0.8). There is a larger deterioration for the case of $K_v \neq 0$ corresponding to light polarized in the plane perpendicular to the electron orbit. The next section discusses whether the AXO can improve the situation for water-cooled mirrors.

3.3. Adaptive X-ray Optics M3

The M3 mirror is an adaptive mirror presenting a predefined elliptical shape. It incorporated a bimorph mechanism able to modify the ellipse in the tangential direction (horizontal) to correct for possible deformations. It will work in close association with a wavefront sensor placed just upstream from it. The diagnostic system will analyze the wave phase received from the wavefront sensor, calculate the distortion as a difference from the measured phase map and the ideal one, compute the correcting mirror profile, calculate the inputs for the adaptive optics

actuators that will shape the mirror to the calculated profile, also accounting for additional effects (backend, dynamic effects).

To simulate the AXO an OASYS widget "WOFRY corrector (reflector)" computes and applies the correction to the wavefront in the following way: i) it extracts the phase from the incident wave $\phi_{inc}(x)$, ii) it calculates the phase spherical wave collapsing to this focal position $\phi_{sph}(x)$, given a distance to the waist (position where we want to focus), iii) calculate the phase difference $\Delta\phi(x) = \phi_{sph} - \phi_{inc}$, and iv) compute the profile height $h(w) = -\Delta\phi(w)/(2k \sin \theta)$.
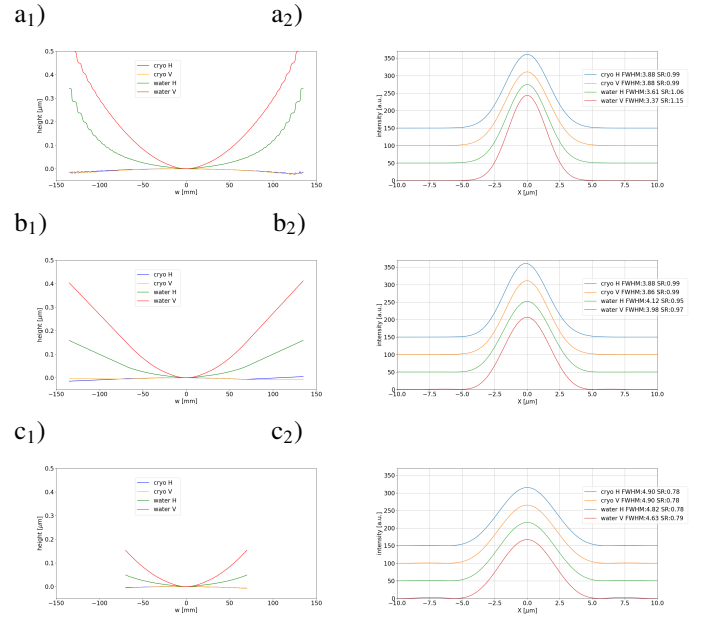
Figure 4
Correction profile on M2 (left) and intensity distribution (right) at the focal position when the different deformations of M1 are corrected by the AXO in M3 using a) ideal correction profile, b) expansion of the ideal profiles as a function of the AXO orthonormal basis and extrapolating the edges to the needed mirror length, and c) expansion of the ideal profiles as a function of the AXO orthonormal basis which defines a shorter the mirror dimension. Note that the intensity profiles have been shifted vertically for clarity.

Fig.4a shows the result using the corrected profiles added to the elliptical shape of the mirror. It is noticeable that the correction works perfectly, arriving to results in intensity distribution and Strehl ratio that are almost identical to case using the undeformed M1. The Strehl ratio has been calculated as the ratio of the peak intensity for the deformed M1 and corrected M3 mirrors over the peak intensity of the undeformed M1 and uncorrected M3. It may look paradoxal that the Strehl ratio is slightly bigger than one for the cases of water-cooled M1. The reason of this apparent contradiction is that M1 becomes convex due to the thermal load (See Figs. 2c$_2$ and d$_2$), therefore M3 sees the source farther away and refocuses it by increasing its curvature thus producing a new optical system with higher demagnification and consequently higher Strehl ratio.

The next question is whether the correcting profiles can be obtained from the real AXO. For that we need a realistic model of the adaptive mirror. We used experimental data from the

study of a AXO mirror prototype manufactured by JTEC and tested at APS [TODO: "reference, experiment number?"]. The mirror length is 140 mm and the AXO mirror has 18 actuators. The mirror profiles obtained by activating a single actuator were measured. The 18 profiles obtained are called influence functions. If we want to set a given arbitrary profile in the mirror, we decompose this profile as a linear combination of the influence functions. The 18 coefficients constitute the input to the actuators. We perform a Gram-Schmidt fitting of the correction profile on an orthonormal basis of AXO influence functions. The basis is computed from the 18 measured influence functions plus a constant term to account for path length changes, and a linear term to provide tilt capabilities. The correction profile is easily expressed as a linear combination of the orthonormal bases. The reconstructed profile built in this way constitutes the "realistic" profile that could be obtained by the AXO. Obviously not every profile could be obtained from the AXO system. For instance, our mirror of length L with 18 actuators could not produce a sinusoidal profile with period smaller than about $L/6$ considering 3 actuators per period.

To accept the full beam the M3 mirror length should be 270 mm which is practically the double of the AXO mirror prototype used. There are three possible scenarios for implementing AXO in M3. The first is get from the manufactures a single mirror which is practically a double replica of the studied prototype, i.e., a length of 2×140 mm with 2×18 actuators. This is the most expensive solution but we expect it would give the best results. We do not study this possibility as we do not have the necessary data. A second possibility is to manufacture a mirror of 270 mm length with the same number of actuators placed in the same geometry. This mirror will be "non-adaptive" at the edges, but we may expect quite good results as usually the central ("adaptive") part receives a large amount of the intensity. A third situation would be to use the existing AXO prototype as M3 mirror.

In Fig. 4 (left column) one can see the different corrective profiles used for M3. Fig. 4a$_1$ presents the ideal corrective profiles as needed for correcting perfectly the wavefront. Fig. 4b$_1$ shows the mirror profiles built from the AXO orthonormal bases and extended to the needed dimension by extrapolating the edges. Fig. 4c$_1$ shows the mirror profiles also decomposed in orthonormal bases but limited to the mirror length of the JTEC prototype measerued. In this case the mirror length is 140 mm and slightly crops the beam. The right column of Fig. 4 shows the intensity distributions obtained with these profiles. The correction obtained using extrapolated profiles (Fig. 4b$_2$) is almost identical to the one obtained using the ideal correcting profiles (Fig. 4a$_2$). It is due to the fact that the edges of the mirror, that are obtained by extrapolation of the profile resulting from the expansion on the orthonormal basis, influence very little the intensity distribution. This results evidence the ability of the AXO to compensate for the surface errors induced by heat load in M1. The case of using directly the existing AXO prototype for this beamline (Fig. 4c$_2$) shows two effects: a reduction of the total intensity as the beam overfills the mirror losing part of its intensity; and also the creation of low intensity diffraction

fringes around X=$\pm6.5\mu$m. These effects contribute to reduce the Strehl ratio to 0.8 independently of the selected cooling conditions.

3.4. Maximum deformation that the adaptive mirror can correct

We study here the limits of how much the AXO in M3 can correct an arbitrary deformation of M1. We simulated profiles to test M1 deformations parametrized in terms of curvature (simulate a "bump" profile) and in terms of spatial frequency (simulate a "cosine").

We created profiles with a "bump" (convex) or anti-bump (concave) (Fig. 5a and b, respectively). For small errors (large curvature radii, above 100 Km), the changes in the intensity distribution are negligeable and the Strehl Ratio is approximately one for all cases, included the uncorrected one. For smaller radii, the Strehl ratio of the uncorrected case drops to zero passing from 100 Km to 100 m, manifesting the need of correction. The adaptive M3 is able to correct the beam and retrieve acceptable values of Strehl ration (close to 0.8 or larger) for radii larger than a Km. In this zone, both for concave or convex deformations, the M3 obtained extrapolating the active zone of the AXO is performing better than the cropped profiles, because the latter reduce the NA increasing the peak width thus decreasing the peak value.

For concave bumps (Fig. 5b) the correction fails around a radius of about 600 m when the deformation in M1 focuses the beam into M3. The M3 mirror fail to compensate M1 radii below one Km, showing the limit of the AXO optics (the correction using ideal profiles, before expanding in the AXO basis is correcting the beam down to radii of 50-100 m).

a)   b)
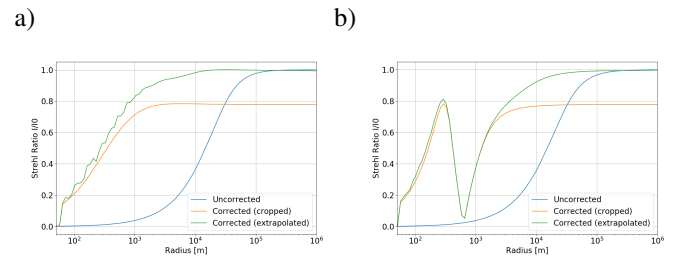
Figure 5
Variation of the Strehl ratio at E=230.88 eV as a function of the deformation radius of curvature in M1 for a) convex curvature (bump) and b) concave curvature (anti-bump). Deformation is compensated with the corrective profiles in M3 expressed as a function of AXO basis for two cases: crop the profile to the AXO dimension and extrapolate the profile outside the AXO mirror (see text).

Next, we studied a periodic deformation in M1 with a form of cosine. The cosine is selected for having a flat top at the mirror center (a sine would give an inflexion). Two cases are analyzed, with deformation amplitude of 50 nm and 30 nm, independently of the period. We present in Fig. 6 the results as a function of the number of ripples found in the mirror length. The period of the cosinusoid is the mirror length over the number of ripples, and zero ripples correspond to the undeformed profile, which defines the normalizetion of Strehl ratio to one. Figs. 6a and b

shows the Strehl ratio as a function of the number of ripples for deformation amplitudes 50 and 30 nm, respectively.

For the uncorrected profiles, the intensity distribution at the focal plane will feature satellite peaks because the deformation acts as a grating. These peaks are more intense for higher deformation amplitudes, thus removing more intensity in the central peak and decreasing the Strehl ratio. That makes that the curves (blue) saturate about a Strehl ration of 0.4 for 50 nm amplitude and about 0.8 for 30 nm. The satellite peaks will separate spatially from the main peak, and the distance increases with the number of ripples (frequency), manifested in a decrease of the Strehl ratio from one (zero ripples) to a constant value at about 2-3 ripples, when the satellites completely separate from the main peak. At this point, the satellites separate more and more when increasing the number of ripples, but this does not modify the Strehl ratio, as the main peak remains constant.

We study first the case of applying an ideal active correction, therefore applying the calculated profile not yet expanded on AXO basis (orange curves in Fig. 6). These corrections work efficiently in the sense that they recover satisfactory values of SR larger than 0.8 independently of the number of ripples. One characteristic is the oscillatory behaviour of the SR. This is originated during the migration of a satellite peak that is very narrow in width: there are positions where it is harder for the AXO to suppress or reduce it with a consequent reduction of the SR. A second feature is that there are cases where the M1 deformation spreads the light at M3, allowing the adaptive correction to achieve an effectively higher numerical aperture (NA). When that happens, the beam is focused to a smaller point in the exit slit plane and the intensity increases, leading to an apparent Strehl Ratio above one. However, integrated power is conserved.

By looking at the corrections produced by the profiles expressed as a function of the AXO ortonormal bases (Fig. 6 (green and red curves) we can appreciate that the SR drops at about 7 ripples. It is because the inability of the limited number of actuators to follow the high frequency distortion. The correction does not work for more ripples. As discussed before for the curvature, the cropped profile reduces both the integrated intensity and also the NA making a shorter and wider peak thus decreasing the SR to unacceptable values (below 0.8). It is remarkable that the correction improves the uncorrected case up to 20 ripples for 50 nm distortion amplitude, but not for the case of small amplitude (30 nm), where in principle no correction is needed because SR is greater than 0.8. The activation of the correction degrades the beam quality instead of improving it. Another feature is that the correction using a extrapolated profile looks very noisy. This is explained by the slope of the extrapolated part (the mirror edges) that is determined by the slope of the edge points, which change drastically versus the number of ripples, thus originating fluctuations in the peak intensity and consequently in the SR.

Therefore correction only works for high profile amplitude and a limited number of ripples (up to 5-7).

a)   b)
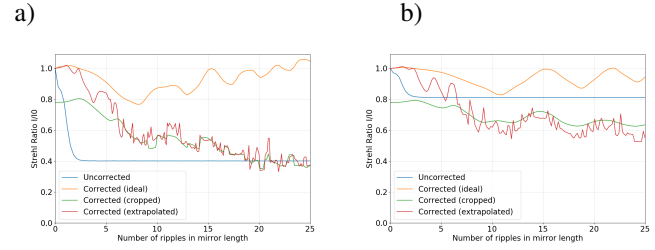
Figure 6
Variation of the Strehl ratio for a deformation in form of cosine and corrections a) deformation amplitude 50 nm, and b) 30 nm.

4. Simulation of the full beamline

For completeness, we simulate the beamline in the vertical plane, featuring a grating monochromator. It consiste in a plane mirror M2 deflecting vertically, and a VLS grating that focus on the focal plane (exit slit). The role of M2 is to adjust the total deflecting angle of the monochromator (constant deflecting angle) when the VLS grating is rotated to change photon energy. For the simulations we can completely ignore it as it is not an optically active element given that i) it does not crop the beam, and ii) its surface is supposed to be perfect. The VLS grating is placed at p=25.73 m from the source and q=4.239 m from the focus. The parameters of the VLS optimized for working at E=230.88 eV are: g_0=300 lines/mm, $g_1 = 0.2698$ mm^{-2}, and g_3=87715 10^{-9} mm^{-3}, and the angles are α=87.127, β=-85.660 and $\theta = (\alpha - \beta)/2$= 86.3936 (c=cos β/ cos α=1.51). The grating is defined by a profile made with step functions of 10 nm height (ruled grating) over a mesh covering the grating length of 150 mm (Fig. 7a). The effect of the grating diffraction is calculated using the model described in Section 2.3.5. The intensity distribution after the grating diffraction is in Fig. 7b which shows a well-focused image with FWHM=4.41μm.

a)   b)
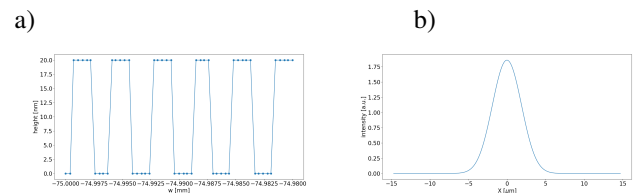
Figure 7
 a) VLS profile used for the simulations (fragment). The total VLS grating length is 150 mm and contains 5 10^5 points. b) Intensity profile at the image position (exit slit) produced by the VLS grating.

The simulations for the vertical plane are combined with the results for the horizontal plane (Fig. 3 or 4) for making a 2D plot. This is done via the outer product of the horizontal and vertical profiles. Fig. 8 shows the results for the worst case of deformation (vertical polarization with water cooling) before and after correction.

a)   b)
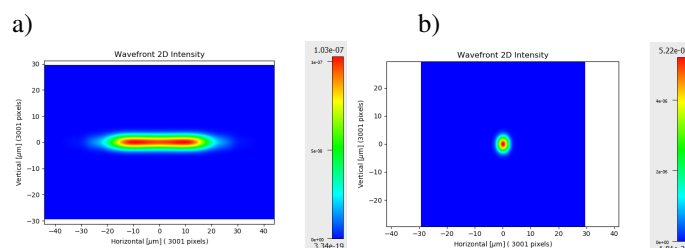
Figure 8

2D intensity at the image position (exit slit plane) obtained for the worst deformation case (vertical polarization and water cooled M1) a) uncorrected image. b) corrected image by using M3 AXO. These images have been obtained combining the vertical profile (Fig. 7)) with the uncorrected and corrected horizontal profiles (Figs. 3 and 4, respectively.)

5. Summary and conclusions

We presented a simple model to simulate a beamline using 1D wavefront propagation. The code developed is fully implemented in the WOFRY package in OASYS. We analyzed the degradation of the beamline parameters, in particular intensity distribution and Strehl ratio, due to the thermal load of the white beam mirror M1. We showed that in the case of cryogenic cooling of the M1 mirror the performances remain very close to the ideal (undeformed) case therefore no correction is needed. However, if the M1 mirror is water-cooled, the induced heat load errors disturb significantly the intensity distribution at the focal plane. These disturbances can be corrected using adaptive X-ray optics, as verified by simulating a realistic model of wavefront correction by Adaptive X-ray Optics. Furthermore, we analyzed the range where the adaptive optics works, by scanning the M1 deformations modelled as curvature (bump or anti-bump) and waviness. We showed that curvatures can be effectively corrected for radii greater than 100 m. The simulations done with wavy profiles show than low spatial frequencies can be corrected, in an optimal mode up to 2-3 ripples per mirror length, and in a satisfactory way (providing SR greater than 0.8) up to 5-7 ripples per mirror length. However, the geometry of the adaptive mirror featuring 18 actuators covering a length of 140 mm makes impossible to correct waviness errors of high spatial frequency (greater than 7 ripples per mirror length). Moreover, the waviness distortions depend on the amplitude, and from the two cases analyzed (50 and 30 nm) we found that deformations of 30 nm and below would not produce SR below 0.8 thus no correction are needed. The proposed model helped to demonstrate the suitability and limitations of using an adaptive mirror to correct for wavefront deformations originated upstream of it.

References

Chubar, O., Berman, L., Chu, Y. S., Fluerasu, S., Hulbert, S., Idir, M., Kaznatcheev, K., Shapiro, D., Shen, Q. & Baltser, J. (2011). *Proc. SPIE*, **8141**, 8141 – 8141 – 10.
URL: *http://dx.doi.org/10.1117/12.892812*

Glass, M., (2017). COMSYL, COherent Modes for SYnchrotron Light.
URL: *http://github.com/mark-glass/comsyl*

Goodman, J. W. (2017). *Introduction to Fourier Optics*. New Yor, USA: w.h.freeman, four ed.

Onuki, H. & Elleaume, P. (2003). *Undulators, Wigglers and Their Applications*. CRC Press.

Rebuffi, L. & Sanchez del Rio, M. (2017*a*). *Proc. SPIE*, **10388**.
URL: *https://doi.org/10.1117/12.2274232*

Rebuffi, L. & Sanchez del Rio, M. (2017*b*). *Proc. SPIE*, **10388**, 10388 – 10388 – 9.
URL: *http://dx.doi.org/10.1117/12.2274263*

Reininger, R., (2001). Srcalc.

Reininger, R. & de Castro, A. (2005). *Nuclear Instruments and Methods in Physics Research Section A: Accelerators, Spectrometers, Detectors and Associated Equipment*, **538**(1), 760 – 770.
URL: *https://doi.org/10.1016/j.nima.2004.09.007*

Sanchez del Rio, M., Celestre, R., Glass, M., Pirro, G., Herrera, J. R., Barrett, R., da Silva, J. C., Cloetens, P., Shi, X. & Rebuffi, L. (2019). *Journal of Synchrotron Radiation*, **26**(6), 1887–1901.
URL: *https://doi.org/10.1107/S160057751901213X*

Schmidt, J. D. (2010). *Numerical Simulation of Optical Wave Propagation*. Bellingham, WA, USA: SPIE Press.

Shi, X., Reininger, R., Sanchez del Rio, M. & Assoufid, L. (2014). *Journal of Synchrotron Radiation*, **21**(4), 669–678.
URL: *https://doi.org/10.1107/S160057751400650X*

Tanaka, T. & Kitamura, H. (2001). *Journal of Synchrotron Radiation*, **8**(6), 1221–1228.
URL: *https://doi.org/10.1107/S090904950101425X*

Temnykh, A., Babzien, M., Davis, D., Fedurin, M., Kusche, K., Park, J. & Yakimenko, V. (2011). *Nuclear Instruments and Methods in Physics Research Section A: Accelerators, Spectrometers, Detectors and Associated Equipment*, **649**(1), 42 – 45. National Synchrotron Radiation Instrumentation conference in 2010.
URL: *https://doi.org/10.1016/j.nima.2010.11.011*

Zhang, L., Barrett, R., Friedrich, K., Glatzel, P., Mairs, T., Marion, P., Monaco, G., Morawe, C. & Weng, T. (2013). *Journal of Physics: Conference Series*, **425**(5), 052029.
URL: *https://doi.org/:10.1088/1742-6596/425/5/052029*